



RESEARCH ARTICLE

10.1002/2013JD020424

Key Points:

- A new lidar technique to derive cloud microphysical properties is applied
- A comparison of droplet sizes of two clouds complies with the Twomey effect
- The influence of the vertical wind speed on cloud microphysics is investigated

Correspondence to:

J. Schmidt,
joerg.schmidt@tropos.de

Citation:

Schmidt, J., A. Ansmann, J. Bühl, H. Baars, U. Wandinger, D. Müller, and A. V. Malinka (2014), Dual-FOV Raman and Doppler lidar studies of aerosol-cloud interactions: Simultaneous profiling of aerosols, warm-cloud properties, and vertical wind, *J. Geophys. Res. Atmos.*, 119, 5512–5527, doi:10.1002/2013JD020424.

Received 25 JUN 2013

Accepted 24 APR 2014

Accepted article online 29 APR 2014

Published online 14 MAY 2014

The copyright line for this article was changed on 23 MAR 2015.

This is an open access article under the terms of the Creative Commons Attribution-NonCommercial-NoDerivs License, which permits use and distribution in any medium, provided the original work is properly cited, the use is non-commercial and no modifications or adaptations are made.

Dual-FOV Raman and Doppler lidar studies of aerosol-cloud interactions: Simultaneous profiling of aerosols, warm-cloud properties, and vertical wind

Jörg Schmidt¹, Albert Ansmann¹, Johannes Bühl¹, Holger Baars¹, Ulla Wandinger¹, Detlef Müller², and Aleksey V. Malinka³

¹Leibniz Institute for Tropospheric Research, Leipzig, Germany, ²School of Physics, Astronomy and Mathematics, University of Hertfordshire, Hatfield, UK, ³B.I. Stepanov Institute of Physics, National Academy of Sciences of Belarus, Minsk, Belarus

Abstract For the first time, colocated dual-field of view (dual-FOV) Raman lidar and Doppler lidar observations (case studies) of aerosol and cloud optical and microphysical properties below and within thin layered liquid water clouds are presented together with an updraft and downdraft characterization at cloud base. The goal of this work is to investigate the relationship between aerosol load close to cloud base and cloud characteristics of warm (purely liquid) clouds and the study of the influence of vertical motions and turbulent mixing on this relationship. We further use this opportunity to illustrate the applicability of the novel dual-FOV Raman lidar in this field of research. The dual-FOV lidar combines the well-established multiwavelength Raman lidar technique for aerosol retrievals and the multiple-scattering Raman lidar technique for profiling of the single-scattering extinction coefficient, effective radius, number concentration of the cloud droplets, and liquid water content. Key findings of our 3 year observations are presented in several case studies of optically thin altocumulus layers occurring in the lower free troposphere between 2.5 and 4 km height over Leipzig, Germany, during clean and polluted situations. For the clouds that we observed, the most direct link between aerosol proxy (particle extinction coefficient) and cloud proxy (cloud droplet number concentration) was found at cloud base during updraft periods. Above cloud base, additional processes resulting from turbulent mixing and entrainment of dry air make it difficult to determine the direct impact of aerosols on cloud processes.

1. Introduction

Field studies of aerosol-cloud interactions (ACI) to quantify the impact of natural and man-made pollution on the evolution of warm (pure liquid) and ice-containing clouds are still challenging [see, e.g., Seifert *et al.*, 2007; Kim *et al.*, 2008; Kanitz *et al.*, 2011; McComiskey *et al.*, 2009; Field *et al.*, 2011; Rosenfeld *et al.*, 2011]. Because of the complexity of the involved processes which take place far away from the ground, the experimental investigation of the influence of aerosol particles on liquid cloud formation [McComiskey and Feingold, 2008] or of the specific impact of a given aerosol type or aerosol mixture on heterogeneous ice nucleation [DeMott *et al.*, 2010; Eidhammer *et al.*, 2010] remains very difficult. Besides a good knowledge of the meteorological conditions and of cloud condensation and ice nuclei concentrations below, within, and above the cloud layer, the impact of upward and downward motions below and within the cloud layers and of turbulent mixing and entrainment processes, particle sedimentation, and cloud seeding effects on cloud evolution has to be known, but these are usually not properly addressed by observations [Ansmann *et al.*, 2009]. This prohibits a clear, unambiguous identification of direct aerosol influences on cloud processes and resulting optical and radiative properties. However, there is a strong need for a better quantification of the role of natural and anthropogenic aerosols on cloud and precipitation formation in the atmospheric system to improve our ability to predict climate change [Forster *et al.*, 2007]. Long-term ground-based remote sensing, short-term airborne in situ aerosol-cloud studies, and global satellite remote sensing contribute to the investigations of aerosol-cloud interactions (ACI). All employed techniques have their advantages and also limitations so that new techniques and methodological approaches need to be developed.

In this paper, we present a novel technique for liquid-cloud ACI studies solely based on lidar. Ground-based active remote sensing provides powerful instrumentation for vertical profiling of aerosol and cloud properties and continuous monitoring of cloud evolution and life cycle [Shupe, 2007; Illingworth *et al.*, 2007; Ansmann *et al.*, 2005, 2009; Martucci and O'Dowd, 2011; Wandinger *et al.*, 2012; Bühl *et al.*, 2013]. For

investigations of the impact of varying aerosol conditions on cloud droplet formation, techniques are desirable that provide information on aerosol microphysical and optical properties such as aerosol particle number concentration (APNC) or particle extinction coefficient just below cloud base as well as cloud microphysical properties such as cloud droplet number concentration (CDNC) or droplet effective radius just above cloud base. In many studies, however, aerosol properties were measured at the surface or at heights far below cloud base and then combined with column-integrated cloud properties [Kim *et al.*, 2003; Feingold *et al.*, 2003a, 2003b, 2006; Garrett *et al.*, 2004; McComiskey *et al.*, 2009]. The respective results then describe the overall effect of aerosol and meteorological influences on cloud processes. The specific role of aerosol particles cannot be properly resolved. Twohy *et al.* [2005, 2013], Lu *et al.* [2007], Ditas *et al.* [2012], Kleinman *et al.* [2012], and Painemal and Zuidema [2013] used airborne platforms to perform in situ observations of aerosol and cloud properties. This approach allows for much more adequate studies of the impact of varying aerosol conditions on cloud formation processes.

We recently introduced the dual-field of view (dual-FOV) Raman lidar method [Schmidt *et al.*, 2013] which permits us to characterize warm (no ice phase), optically thin, layered clouds in terms of height profiles of single-scattering droplet extinction coefficient, CDNC, droplet effective radius, and liquid water content. By implementing two multiple-scattering channels (elastic and nitrogen Raman multiple-backscatter channels) into a state-of-the-art multiwavelength Raman/polarization lidar [Mattis *et al.*, 2004, 2008; Müller *et al.*, 2005], we are now able to combine a detailed aerosol characterization in terms of accumulation-mode APNC, effective radius, and aerosol particle extinction coefficient [Müller *et al.*, 1999; Ansmann and Müller, 2005] with a respectively detailed cloud microphysical characterization. A clear, unambiguous detection of the cloud base is also possible by using the backscatter information from the Raman multiple-scattering channels. An accurate cloud base determination is required in our ACI studies but hampered or masked by a strong increase of light backscattering caused by water-uptake by aerosol particles when using the standard backscatter lidar method.

The limitations of lidar applications in cloud studies should also be mentioned in the beginning. Lidar observations are restricted to optically thin clouds. Cloud top detection and full profiling throughout warm-cloud layers is only possible for cloud optical depths <2.5 – 3.0 and respective liquid water paths (LWPs) of less than about 50 g/m^2 . Furthermore, the presence of intense drizzle virga may disturb aerosol characterization below cloud base. Our dual-FOV lidar is only applicable to clouds above 1.3 km height [Schmidt *et al.*, 2013]. To partly reduce these two shortcomings, we used colocated cloud radar observations for drizzle and cloud top identification.

The instrumental and technical details of the novel dual-FOV Raman lidar method are discussed by Schmidt *et al.* [2013]. In this first part of a series two papers (Part II is in preparation and will present the statistical analysis of about 30 cloud layer observations), we begin with three observational cases to illustrate the applicability of the new lidar approach in warm-cloud research. By adding simultaneously measured Doppler lidar profiles of the vertical-wind component at cloud base, we then present two illustrative cases where we investigated the impact of different aerosol levels on the cloud droplet extinction coefficient and cloud microphysical properties, and this separately for updraft and downdraft periods. In this way, we can discuss the impact of vertical motion and related turbulent mixing on these interactions. Our findings corroborate the hypothesis [Feingold *et al.*, 2003a, 2003b; Kim *et al.*, 2008] that vertical motion has a strong impact on ACI and that entrainment processes severely complicate studies of the influence of varying aerosol levels on cloud droplet formation as will be discussed in section 3.3.

We start with a brief description of the lidars, cloud radar, and microwave radiometer used in this study (section 2.1). Details of cloud-retrieval aspects of the novel dual-FOV Raman lidar are given in section 2.2. Key findings of our 3 year observations are illustrated by several cases presented in section 3. The first study deals with the comparison of altocumulus evolution in clean and polluted air (section 3.1). The second case illuminates explicitly the potential of the dual-FOV lidar to provide simultaneously APNC and CDNC information (section 3.2). The third and central case study includes the Doppler lidar observations of the vertical wind component at cloud base and in the lower part of a cloud layer (section 3.3). Based on these observations, the complications and blurring effects caused by updrafts, downdrafts, and turbulent mixing in studies of aerosol-cloud interactions are discussed. Concluding remarks are given in section 4.

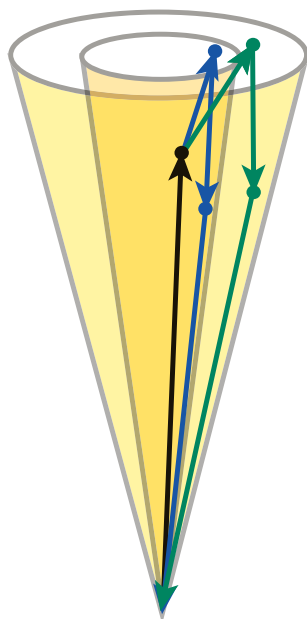


Figure 1. Geometry and principle of dual-FOV measurements. Yellow: Inner, circular FOV. Light yellow: Outer, annular FOV. Scattering by larger droplets leads to smaller scattering angles in forward direction and thus to a stronger signal in the inner FOV (blue scattering process). Smaller droplets cause larger forward scattering angles and thus a signal increase in the outer FOV (green scattering process).

2. Instrumentation and Cloud Data Analysis

2.1. LACROS

The Leipzig Aerosol and Cloud Remote Observation System (LACROS, 51.3°N, 12.4°E) [Wandinger *et al.*, 2012] of the Leibniz Institute for Tropospheric Research (TROPOS), Leipzig, Germany, was established in 2011. Cornerstones of LACROS are the multiwavelength Raman/polarization lidar MARTHA (Multiwavelength Atmospheric Raman Lidar for Temperature, Humidity, and Aerosol Profiling) which is part of EARLINET (European Aerosol Research Lidar Network) [Mattis *et al.*, 2004, 2008, 2010; Wandinger *et al.*, 2004; Schmidt *et al.*, 2013], the wind Doppler lidar WILI [Engelmann *et al.*, 2008; Bühl *et al.*, 2012], the 35 GHz cloud radar MIRA35 [Bühl *et al.*, 2013], and the microwave radiometer HATPRO (Humidity And Temperature Profiler) [Rose *et al.*, 2005].

MARTHA is a powerful Raman lidar and was upgraded to perform dual-FOV Raman lidar measurements for the retrieval of cloud microphysical properties in 2008 [Schmidt *et al.*, 2013]. A Nd:YAG laser emits radiation pulses at the wavelengths of 355, 532, and 1064 nm with pulse energies of 0.3, 0.6, and 0.5 J, respectively, and a repetition rate of 30 Hz. The receiver of MARTHA consists of a 0.8 m diameter telescope and a beam separation unit with 12 detection channels. Particle backscatter coefficients at 355, 532, and 1064 nm and extinction coefficients at 355 and 532 nm can be determined from these lidar observations [Ansmann *et al.*, 1990, 1992; Ansmann and Müller, 2005]. By applying the method of inversion with regularization with constraints [Müller *et al.*, 1999; Wandinger *et al.*, 2002; Ansmann and Müller, 2005] to the set of spectrally resolved particle backscatter and extinction coefficients, microphysical properties of the aerosol particles in terms of volume and surface concentration, effective radius, and APNC (covering accumulation and coarse-mode particles with diameters of 0.1–10 μm) can be derived.

The novel dual-FOV Raman lidar technique makes use of two receiver FOVs. Raman scattered light with a wavelength of 607 nm is detected with a conventional, circular FOV and an annular, outer FOV encompassing the inner, circular FOV. The measurement geometry is illustrated in Figure 1. In the case of lidar measurements in clouds, multiply scattered light is detected due to the pronounced forward scattering peak of the phase function of cloud droplets. The width of the forward scattering peak correlates unambiguously with the size of the scattering droplets. As the forward scattering angles determine the ratio between the signals of the inner and outer FOV, the ratio of the signals from the inner and outer FOV contains information about cloud droplet size up to 50 g/m^3 .

The new aspect introduced here is the detection of light which is forward scattered by cloud droplets and Raman backscattered by nitrogen molecules. As illustrated in Figure 2, the key point of the technique is that Raman backscattering from nitrogen molecules is nearly isotropic for scattering angles close to 180° so that the angular distribution of the incoming light depends on the forward scattering by droplets only. In strong contrast, the conventional multiple-scattering lidar technique is based on the measurement of elastically backscattered laser light [Bissonnette and Hutt, 1995; Bissonnette *et al.*, 2002; Bissonnette, 2005]. Forward scattering and backscattering by cloud droplets influence the angular distribution of the incoming light but both scattering processes depend on drop size in a different way (see Figure 2, green and blue curves). This prohibits a clear straightforward determination of the drop size characteristics.

To be capable of performing dual-FOV cloud measurements in an extended altitude range from 1.3 to 6 km height, the receiver of MARTHA is set up in the way that the measurement geometry can be easily optimized regarding the contrast of the multiple-scattering effects in the two channels by exchanging the field stop [Schmidt *et al.*, 2013]. FOV pairs of 0.28 and 0.78 mrad (for clouds above about 4 km height), of 0.5 and 2.0 mrad (for clouds from about 2.7 to 4 km height), and of 0.78 and 3.8 mrad (for clouds with base <2.7 km) are used [Schmidt *et al.*, 2013]. Due to the small Raman scattering cross section, the dual-FOV Raman lidar measurements are restricted to nighttime hours.

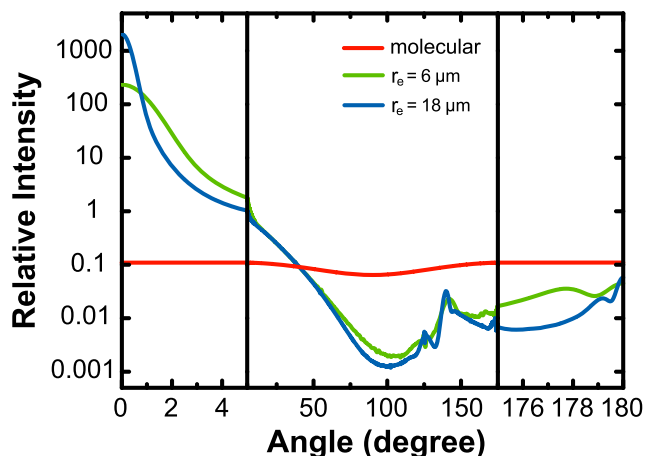


Figure 2. Scattering phase function for cloud droplet ensembles (gamma distributions after *Deirmendian* [1969] and *Plass and Kattawar* [1971]) with effective radius of 6 μm (green) and 18 μm (blue). Forward (0–5°) and backward (175–180°) scattering angle ranges are enlarged. For comparison, the scattering phase function for air molecules (red, Rayleigh or Raman scattering) is almost wavelength-independent at forward and backscattering angles.

The Doppler wind lidar WILI operates at a wavelength of 2022 nm and emits laser pulses of 450 ns (140 m) length and 1.5 mJ pulse energy with a pulse repetition rate of 750 Hz [Engelmann *et al.*, 2008; Bühl *et al.*, 2012]. Vertical and temporal resolutions are 75 m and 2 s, respectively. The uncertainty in the determination of the vertical-wind component is of the order of 10 cm/s. WILI observations were mainly used in our study to separate regions with upward and downward motions. To remotely sense the same volume with WILI and MARTHA, both systems were located within a distance of less than 10 m, and both lidars were pointing exactly to the zenith.

The cloud radar is used here only for drizzle detection and cloud top identification to corroborate the lidar observations in cases with optically dense clouds. The HATPRO microwave radiometer allows us to estimate LWP [Rose *et al.*, 2005] which can be compared with the column-integrated liquid water content (LWC) obtained from the dual-FOV Raman lidar observations (as explained in the next section). The uncertainty in the HATPRO LWP is about 15–30 g/m² [Westwater *et al.*, 2001; Crewell and Löhnert, 2003; Gaussiat *et al.*, 2007; Ebell *et al.*, 2011]. For a distinct reduction of the relative error to about 10%, the LWPs from HATPRO were calibrated to 0 g/m² in cloud-free regions indicated by lidar or ceilometer before or after the passage of layered clouds [Gaussiat *et al.*, 2007].

2.2. Retrieval of Cloud Microphysical Parameters

The novel dual-FOV Raman lidar technique permits the derivation of profiles of the cloud droplet effective radius r_e ($3V/A$ with droplet volume concentration V and surface area concentration A) and cloud droplet (single-scattering) extinction coefficient α [Malinka and Zege, 2007; Schmidt *et al.*, 2013]. The effective radius is the third moment (LWC) over the second moment (α). LWC is given by $2/3\rho r_e(z)\alpha(z)$ with water density ρ . No assumptions about cloud properties (e.g., adiabatic profile of LWC or certain cloud droplet size distribution) have to be made in our dual-FOV lidar approach. The measured width (in terms of scattering angle) of the light-scattering defraction peak is unambiguously related to the effective droplet radius r_e . The range of observable effective radii is about 1.5–30 μm [Schmidt *et al.*, 2013], in agreement with simulation studies of Veselovskii *et al.* [2006]. The uncertainties in the derived quantities (as shown as error bars in section 3) are obtained by input variation of the measured signals in both FOVs, comparison of the results when different height resolutions are applied in the computations, and by considering uncertainties in the retrieved cloud base and cloud top heights [Schmidt *et al.*, 2013]. The resulting uncertainties in the presented cloud properties are mostly of the order of 10% to 30%.

To study the relationship between CDNC and the aerosol load (in terms of APNC or aerosol particle extinction coefficient α_p), we compute CDNC (denoted as N in the following formula) from [Brennguier *et al.*, 2000]

$$N = \frac{\alpha}{2\pi r_s^2}, \tag{1}$$

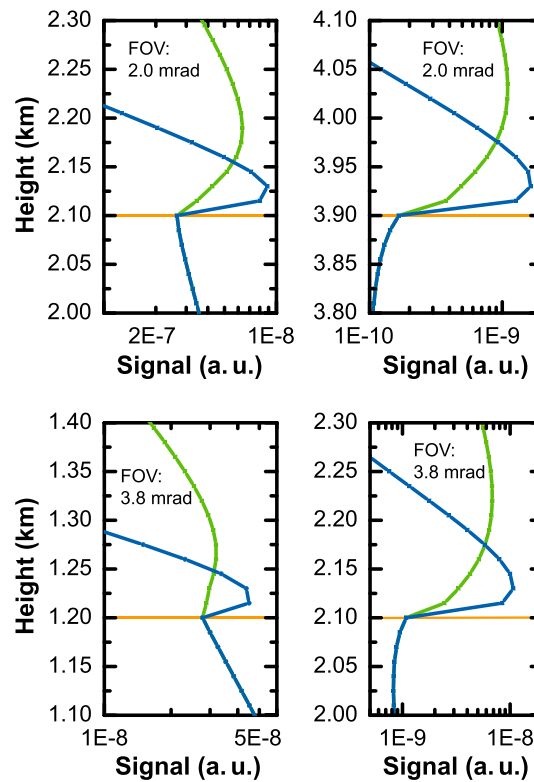


Figure 3. Simulated Raman signals (in arbitrary units, a.u.) from the outer-FOV (multiple-scattering) channel with FOV of (top) 2.0 mrad and (bottom) 3.8 mrad for clouds with droplet effective radii of (left) 8 μm and (right) 3 μm and extinction coefficients of 5 (green) and 20 km^{-1} (blue). Cloud base heights at 1.2, 2.1, and 3.9 km are indicated by orange lines. All simulations show a strong, unambiguous increase of the signal at cloud base due to multiple scattering by cloud droplets.

[2006] compiled a list of k -values for stratiform clouds based on a literature review. The k range of 0.75 ± 0.15 well represents the values found for continental air masses. In the following, we use 0.75 for l in equation (4) and assume an uncertainty in l of 20% in the computation of the uncertainty in N after equation (4).

2.3. Retrieval of Cloud Base Height

The detection of the cloud base height with lidar is often masked by a strong increase of the backscatter coefficient by a factor of >5 below cloud base due to the rapid growth of aerosol particles by water uptake. In the case of the dual-FOV Raman lidar, the outer-FOV signals (multiple-scattering channels) can be used to identify the true cloud base (at which relative humidity reaches the 100% level). Significant multiple-scattering occurs only if the aerosol particles become activated. Even large aerosol particles after water uptake are not able to produce a significant multiple scattering signal. This potential to unambiguously detect cloud base height is illustrated in Figure 3. The simulations of the Raman signals shown in Figure 3 are based on the model of *Malinka and Zege* [2003]. In all simulations, the Raman signal from the outer FOV strongly increases at cloud base. The slope of the increase differs with the measurement geometry and cloud properties. Water-uptake by aerosol particles is considered in the simulations and, as shown, does not affect the precise cloud base detection.

3. Observations

The first two observational studies illuminate the influence of observed aerosol conditions close to cloud base on the microphysical properties of optically thin layered clouds. The third case study includes measurements of the vertical wind component with Doppler lidar and the comparison of aerosol-cloud relationships

with the surface mean droplet radius $r_s = (\bar{r^2})^{1/2}$. N is the zeroth moment of the droplet size distribution. To obtain the unknown surface mean radius r_s from the retrieved effective radius r_e , we assume a modified gamma distribution for the shape of the droplet size spectrum. According to in situ measurements [*Miles et al.*, 2000], gamma distributions well describe most cloud drop size distributions. The modified gamma distribution is defined by

$$n(r) = \frac{N}{\Gamma(\nu)} r^{\nu-1} \lambda^\nu \exp(-\lambda r) \quad (2)$$

with the parameters $\nu, \lambda > 0$. The relationship between r_s and r_e is then given by

$$r_s^2 = \frac{\nu(\nu+1)}{(\nu+2)^2} r_e^2 = l r_e^2, \quad (3)$$

with the factor $l = \nu(\nu+1)/(\nu+2)^2$ so that N can be obtained from (see equations (1) and (3)):

$$N = \frac{\alpha}{2\pi l r_e^2}. \quad (4)$$

Miles et al. [2000] set up a database from various in situ measurements of droplet size distributions of low-level stratus clouds. The fit of a modified gamma distribution to the size distributions obtained from measurements in continental air masses yielded $\nu = 8.7 \pm 6.3$ and thus a mean value of l of 0.74 within a range from 0.42 to 0.83.

Similar to equation (4), an alternative approach can be obtained by starting from $k = r_v^3/r_e^3$ with the volume mean radius r_v [*Martin et al.*, 1994] so that equation (4) is then given as a function of k instead of l . For continental air masses, *Lu and Seinfeld*

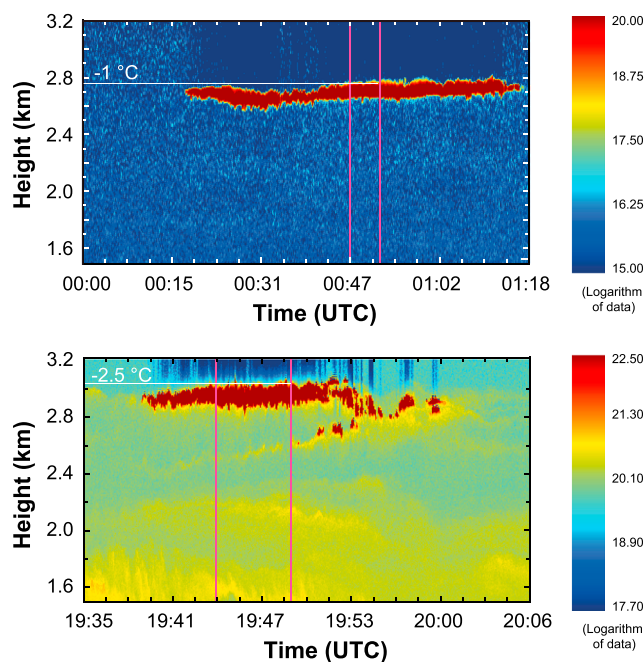


Figure 4. Altocumulus layer (in red) observed with MARTHA on (top, clean conditions) 26 July 2011 and (bottom, polluted conditions) 5 September 2011. The range-corrected signal (arbitrary units) at 532 nm from the inner FOV is shown. The time period used for the cloud analysis is indicated by pink vertical lines. Cloud top temperatures (in white) are derived from GDAS (Global Data Assimilation System [Kanamitsu, 1989]) temperature profiles for grid point Leipzig at 00:00 UTC on 26 July 2011 and 21:00 UTC on 5 September 2011.

during updraft and downdraft periods. This study is a useful guide for future studies of aerosol-cloud interactions by showing the consequences of organized vertical motions in updrafts and turbulent mixing on ACI investigations.

3.1. Altocumulus in Clean and Moderately Polluted Air

Figure 4 shows two observations of layered clouds. They formed at free tropospheric heights above 2.5 km in clean and polluted air. On 26 July 2011, the air mass was advected from Greenland over Iceland and the North Atlantic (including the North Sea) toward Germany. This altocumulus layer was formed under background aerosol conditions. On 5 September 2011, a haze layer reaching to about 3 km height was present. This aerosol originated from polluted regions of North America and crossed polluted parts of western Europe before arriving at Leipzig, Germany, according to backward trajectory analysis.

Figure 5 presents profiles of temporal mean aerosol particle extinction and backscatter coefficients on these 2 days with very different aerosol loads. The basic mean lidar signal profiles were

smoothed with 60 m (backscatter coefficients) and 500–900 m window length (extinction coefficient) before the computation of the optical properties. Clear-air (Rayleigh) backscatter-coefficient calibration at heights above 5 km was performed during cloud-free periods. On the clean day (26 July) an average extinction coefficient of 10 Mm^{-1} (or 0.01 km^{-1}) for the green height area in Figure 5 was determined. Because the relative humidity was 70%–80% in the green area according to nearby radiosonde ascents, the dry-aerosol extinction coefficient was probably below 8 Mm^{-1} . The haze extinction coefficients on 5 September ranged from 20 to 50 Mm^{-1} in the green area (mean value of 30 Mm^{-1}). Relative humidities were mostly 50%–70% in the green area and indicated less water uptake by the particles. The dry-aerosol particle extinction coefficients were probably 10%–20% lower than the one shown. The Raman lidar observations further yielded particle extinction to backscatter ratios (lidar ratios) of 60–65 sr in the green areas on 5 September. These lidar ratios are typical for aged fine-mode particles of anthropogenic origin [Müller *et al.*, 2007].

According to the multiple-scattering signal profiles in Figures 5b and 5d, cloud bases were at 2.55 km (26 July) and 2.8 km (5 September) and thus 75 m (26 July) to 165 m (5 September) above the height at which the particle backscatter coefficients begin to strongly increase. Fluctuations in the cloud base height as well as water uptake by particles contributed to the shift of the backscatter-coefficient minimum by 75–165 m below mean cloud base. The multiple-scattering signal is less sensitive to cloud base variations as our simulations show and always provides robust information on the base of the cloud layer.

According to our cloud radar observations, cloud top was at 3.0 km height on 5 September. In agreement with the lidar measurements virga of drizzle droplets were not observed. The radar indicated a cloud depth of 100–150 m, in contrast to the lidar observations (cloud depth of 200 m). The cloud layer on 26 July 2011 was not detected with the cloud radar, which is almost insensitive to droplets with radii $<10 \mu\text{m}$. As shown in Figure 6, the droplet effective radius was $<10 \mu\text{m}$ throughout the cloud layer on 26 July.

An overview of the lidar-derived cloud optical and microphysical properties for the 2 days is presented in Figure 6. The altocumulus layers were measured with FOV pairs of 0.78 and 3.8 mrad (26 July) and 0.5 and

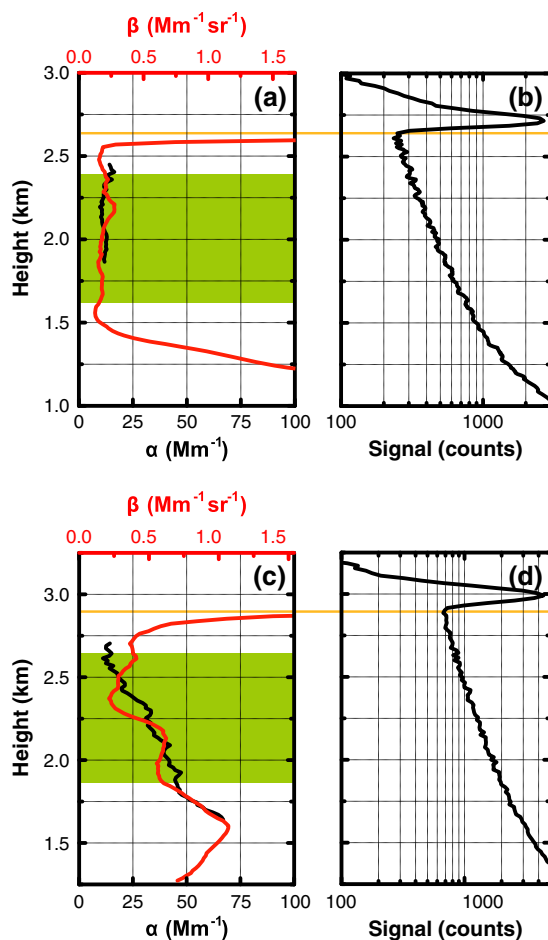


Figure 5. Profiles of particle extinction coefficient (black) and backscatter coefficients (red) below the clouds derived from mean lidar signal profiles for the periods from (a) 00:00 to 01:18 UTC on 26 July 2011 (Figure 5a) and 19:35 to 20:06 UTC on 5 September 2011, excluding the period from 19:49–19:58 UTC (Figure 5c). The mean aerosol optical properties in the green areas are assumed to represent the aerosol conditions during cloud formation (i.e., at cloud base). (b, d) Signal profiles from the outer FOV at 607 nm (multiple-scattering channel) indicating the cloud base heights (orange, horizontal lines) at 2.65 km height (Figure 5b) and 2.9 km height (Figure 5d).

cleaner environment shows a much lower CDNC in the lowest 50 m of the cloud. The CDNC difference (just above cloud base) between the two cloud cases is of the order of a factor of 3–4. A factor of 3 describes the difference in the aerosol optical properties.

We checked also the quality of our lidar-based LWC retrieval by comparing the height-integrated LWC values with the LWPs measured with the microwave radiometer HATPRO. Table 1 provides an overview of LWPs derived from HATPRO and our lidar observations for all cloud cases discussed here. The column-integrated LWCs match the LWPs from HATPRO for all clouds except for the cloud measured on 5 September 2011, where the LWP from HATPRO is much larger than the column-integrated LWC. As mentioned in section 2, the relative error of the HATPRO-derived LWP is about 10%. Different viewing geometries of HATPRO and the lidar in combination with horizontal LWP inhomogeneities may be partly responsible for the larger deviations in Table 1. Our cloud measurements (HATPRO, lidar) show at all low LWPs from about 5–33 g m⁻².

To provide a more quantitative analysis of our observations, we computed several ACI parameters [Feingold *et al.*, 2001; Garrett *et al.*, 2004; McComiskey and Feingold, 2008; McComiskey *et al.*, 2009]. The indirect-effect

2.0 mrad (5 September). For the analysis of cloud microphysical properties, we averaged dual-FOV Raman signal profiles for periods with almost constant cloud base height. These signal averaging periods are indicated by pink vertical lines in Figure 4. At both days, droplet extinction coefficients were 5–15 km⁻¹ about 50 m above cloud base, but the effective radii of the droplets were 6±3 μm on the clean day and 4±1.5 μm on the polluted day. LWCs were of similar magnitude just above cloud base. The LWC profiles are close to respective adiabatic LWC profiles (not shown) up to 2710 m (26 July) and 2960 m (5 September) when taking the uncertainties (error bars shown in the figure) into account. The computation of adiabatic LWC profiles is explained below (when Figure 13 is discussed). Deviations of the observed LWC profiles from the adiabatic ones above 2710 m (26 July) and 2960 m (5 September) must be interpreted with caution. Descending cloud parcels containing a comparably high liquid water amount may have contributed to such super adiabatic LWC profiles. However, it is more likely that the results are erroneous because of the large uncertainties in the lidar retrieval.

The clear difference between the cloud droplet effective radii on 26 July and 5 September 2011 throughout the lower half of the cloud agrees well with the predictions of the first indirect aerosol effect, namely that the effective radius decreases with increasing aerosol load.

In Figure 6 (right panels), the CNDC profiles are shown. The comparably large uncertainties in the derived CDNC values result from the strong impact of the uncertainty in the effective radius according to equation (4). The influence of the uncertainties in cloud extinction coefficient and in the gamma size distribution parameter *l* is comparably small. The cloud embedded in the

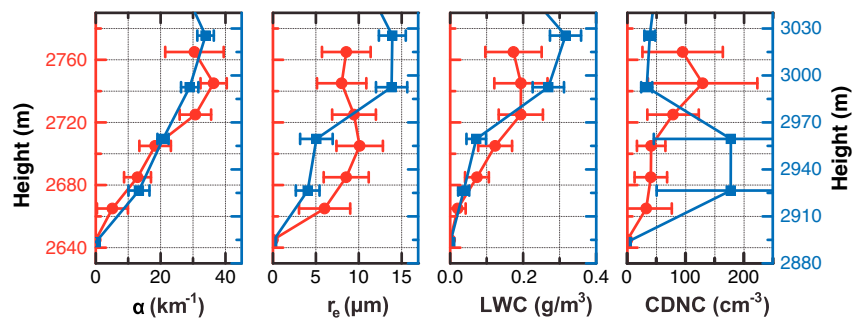


Figure 6. Cloud microphysical properties in terms of droplet single-scattering extinction coefficient α , effective radius r_e , liquid water content (LWC), and cloud droplet number concentration (CDNC) for the clean case (26 July 2011, red profiles) and polluted conditions (5 September 2011, blue profiles). Error bars indicate the uncertainties (1 standard deviation). They are computed with the dual-FOV lidar retrieval scheme (α , r_e) and by applying the law of error propagation to the LWC equation (defined in section 2.2) and equation (4) (CDNC).

parameter $ACI_r = -\partial \ln(r_e) / \partial \ln(\alpha_p)$ for constant LWC with the aerosol particle extinction coefficient α_p (index p here to distinguish from cloud droplet extinction α) describes the relative change of the droplet effective radius r_e with a relative change in the haze aerosol load parameter α_p at constant LWP (or LWC) conditions. The requirement of similar cloud LWP and cloud-base LWC values was well fulfilled for these two cases. The aerosol particle extinction coefficient α_p was found to be the most robust aerosol parameter (e.g., compared to inversion retrieval products such as N_{acc} , see section 3.2). Effects of particle water uptake on the measured or corrected ambient α_p values may introduce uncertainties of the order of 25% in the derived ACI values.

Similar to ACI_r , the nucleation-efficiency parameter can be defined, $ACI_N = d \ln(N) / d \ln(\alpha_p)$, and describes the relative increase of the droplet number concentration with increasing aerosol load. ACI_r is equal to $3 ACI_N$ (for constant LWC) according to the $r_e \propto N^{-1/3}$ relationship. ACI_r and ACI_N can vary between zero (no dependence) and 0.33 and 1 (linear increase of CDNC with APNC), respectively. By using the cloud effective radii at the lowest height above cloud base of $4 \mu\text{m}$ on 5 September and $6 \mu\text{m}$ on 26 July 2011 and the mean values of the aerosol particle extinction coefficient below the cloud layers of 10 Mm^{-1} on 26 July and 30 Mm^{-1} on 5 September, we yield $ACI_r = 0.37$. If we assume dry-particle extinction coefficients of around 7.5 Mm^{-1} (26 July) and 26 Mm^{-1} (5 September) according to our discussion above, we obtain the maximum possible value of $ACI_r = 0.33$ in this case. Because of the large uncertainties in the derived CDNCs of 75%–100%, ACI_N values are not presented. If we use the cloud mean values of r_e ($8.3 \mu\text{m}$ on 26 July, $9 \mu\text{m}$ on 5 September), as usually done in many previous studies of ACI [Garrett et al., 2004; Feingold et al., 2006; McComiskey et al., 2009], we obtain a negative

ACI_r of -0.08 . It should be mentioned here that the ACI values computed above from cloud mean effective radii differ insignificantly from the ones obtained when explicitly LWP and cloud optical depth information is used to estimate the column-integrated effective radii in the respective ACI_r estimation. These cloud column values are usually derived when passive remote sensing is involved in ACI studies.

Table 1. Comparison of LWP From HATPRO and Integrated LWC From Dual-FOV Raman Lidar Measurements for All Clouds Presented in This Study

| Date | LWP From HATPRO (g/m ²) | LWC From Lidar (g/m ²) |
|-----------------------------|-------------------------------------|--|
| 26 July 2011 | 8.4 ± 4.2 | 15.2 ± 8.6 |
| 15 August 2011 | 21.0 ± 7.3 | 27.7 ± 9.4 (up) ^c 31.6 ± 7.5 (down) ^c |
| 29 August 2011 | 11.8 ± 6.6 | 12.9 ± 4.6 (up) ^c 7.6 ± 2.4 (down) ^c |
| 5 September 2011 | 33.2 ± 3.1 | 14.7 ± 3.3 |
| 29 August 2012 ^a | 5.4 ± 5.3 | 9.8 ± 4.8 |
| 29 August 2012 ^b | 10.3 ± 10.0 | 11.0 ± 4.8 |

^aCloud with base at 3.7 km height.

^bCloud with base at 3.3 km height.

^cUp and down denote up and downdraft periods.

3.2. Link Between CDNC and APNC at Cloud Base

The combination of multiwavelength aerosol Raman lidar and dual-FOV lidar allows us for the first time to derive APNC (aerosol particle number concentration, here the concentration of accumulation-mode particles with radii

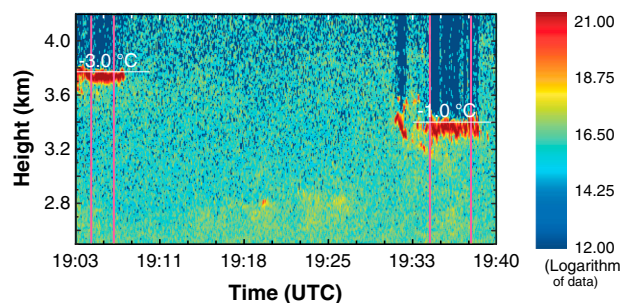


Figure 7. Altocumulus layers (in red) observed on 29 August 2012. The range-corrected signal (arbitrary units) at 532 nm from the inner FOV is shown. The two layered clouds formed at 3.3 and 3.7 km height in moderately polluted air. The time periods used for the cloud analysis are indicated by pink vertical lines. Cloud top temperatures (in white) are derived from GDAS data for grid point Leipzig at 18:00 UTC. Aerosol particle properties shown in the next figure are calculated from the lidar observations during the cloud-free period from 19:15 to 19:30 UTC.

>50 nm) at heights below the cloud layer and CDNC just above cloud base. Figure 7 shows two cloud layers at 3.3 and 3.7 km height and a cloud-free period from 19:10–19:30 UTC. In Figure 8(a) and (b), the determined backscatter and extinction coefficients of the aerosol particles for this cloud-free period are shown. In the case of the extinction profiles, the basic Raman signals were vertically smoothed with 600–900 m window length to reduce the statistical uncertainty to about 20%. In contrast, the backscatter coefficients are given with 60 m resolution. To obtain the aerosol particle concentration of the accumulation and coarse modes (APNC or N_{acc} , retrieval diameter range from 0.1–10 μm) and the corresponding parti-

cle effective radius r_{eff} in Figure 8(c), we applied the method of inversion with regularization as explained in section 2.1.

The optical properties in Figures 8a and 8b indicate moderately polluted aerosol conditions up to 3–4 km height. The 532 nm particle extinction and backscatter coefficients were $<20 \text{ Mm}^{-1}$ and $<0.5 \text{ Mm}^{-1} \text{ sr}^{-1}$ (lidar ratio was about 40 sr) above 3.2 km height where the clouds formed. The APNC was high with values of around 1500 cm^{-3} below 3 km height. In the height range from 3.2 to 3.8 km, where the cloud layers occurred, an APNC of about 300 cm^{-3} with an uncertainty of approximately 100 cm^{-3} was derived. The aerosol particle effective radius was low (about 100 nm) and indicated the dominance of fine-mode haze. It must be emphasized that lidar-derived APNC considers aerosol particles with diameters from 100 nm to 10 μm at ambient humidity conditions. In contrast, in situ aerosol measurements usually provide dry-particle information. In situ measured APCNs then include particles with dry-particle diameters $>100 \text{ nm}$. Our APNC

values for ambient aerosol conditions therefore may include a significant amount of particles with dry-particle diameters as small as 70–80 nm, and correspondingly our ambient APNCs may be considerably larger than the in situ measured dry-particle APNCs.

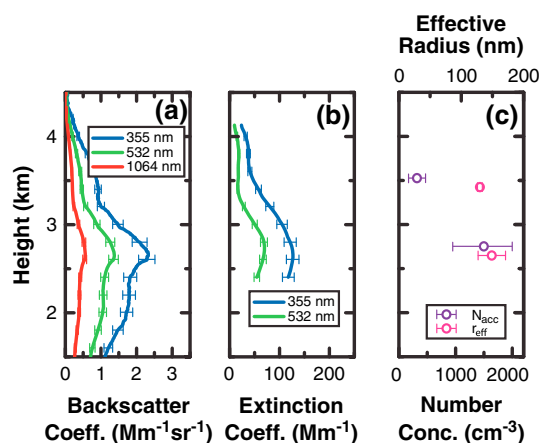


Figure 8. (a) Raman-lidar-derived aerosol particle backscatter coefficient for three laser wavelengths, (b) aerosol particle extinction coefficient for two wavelengths, and (c) aerosol particle number concentration (N_{acc} , particles with radius $>50 \text{ nm}$) and aerosol particle effective radius (r_{eff}) obtained by means of a lidar inversion scheme applied to the optical properties (a,b) for two layers from 2.45 to 2.95 km and 3.0 to 4.0 km height. Mean aerosol properties for 29 August 2012, 19:15–19:30 UTC are shown. This period is used to characterize the aerosol properties in the period between the two cloud layers shown in Figure 7.

Figure 9 shows the microphysical properties of the two cloud layers. The cloud extinction coefficients and the LWC values are significantly higher in the upper cloud layer than in the lower one. Both LWC profiles significantly deviate from the respective adiabatic LWC profiles, except for the lowest retrieval height above cloud base. Again, this may be widely the result of large uncertainties in the lidar retrieval.

Effective radii are similar in both clouds in Figure 9. The CDNC values are rather uncertain because of the relatively large errors in the cloud droplet effective radii of 25%–40% and a respective error contribution to the CDNC relative uncertainty of 50%–80%. The colocated cloud radar only identified the lower cloud layer and did not indicate any drizzle formation.

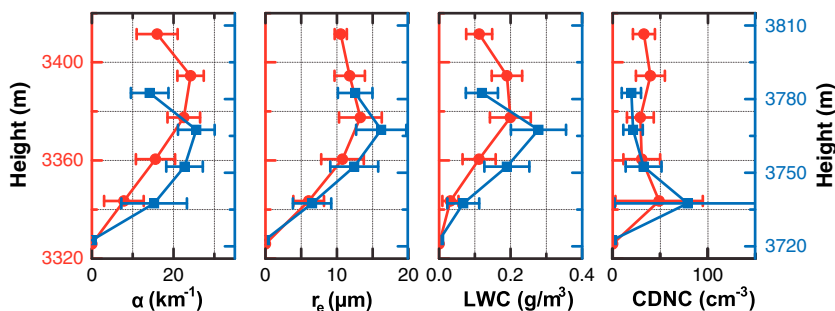


Figure 9. Same as Figure 6 except for 29 August 2012, 19:04–19:07 UTC average (upper cloud, blue) and 19:34–19:39 UTC average (lower cloud, red).

We leave out a further investigation of the aerosol influence on cloud drop evolution in terms of ACI_r and ACI_N in this cases with almost similar aerosol conditions for both detected cloud layers. Nevertheless, the APNC and CDNC information can be used to estimate how many of the aerosol particles of the accumulation and coarse-mode particles (0.1–10 μm diameter range) served as cloud condensations nuclei (CCN). According to Figures 8 and 9, we see that CDNC is of the order of 40–80 cm^{-3} in the lowest part of the cloud layers, whereas the APNCs below the cloud layers are around 300 cm^{-3} so that roughly 15%–25% of the accumulation particles (for ambient humidity conditions) probably served as CCN in this measurement case.

3.3. Influence of Updraft and Downdraft Motions

In our last and central case study we discuss the impact of updrafts and downdrafts, turbulent mixing, and entrainment of dry air on the evolution of the microphysical characteristics of layered clouds. On 15 August 2011, combined Doppler lidar and dual-FOV Raman lidar observations were performed. A 150–200 m thick stable cloud layer was present for more than 2 h. The cloud radar detected the uppermost 50–100 m of the cloud deck with top heights at 3.0–3.1 km height. Drizzle was not observed. Figure 10 provides dual-FOV lidar information on aerosol conditions and cloud extent. The cloud base was rather constant over the 2 h period and increased by about 50–100 m after the first 20 min of observation toward the end. The profiles of aerosol particle backscatter and extinction coefficients below the cloud base in Figure 10 (right) are thus not disturbed by any cloud base variation.

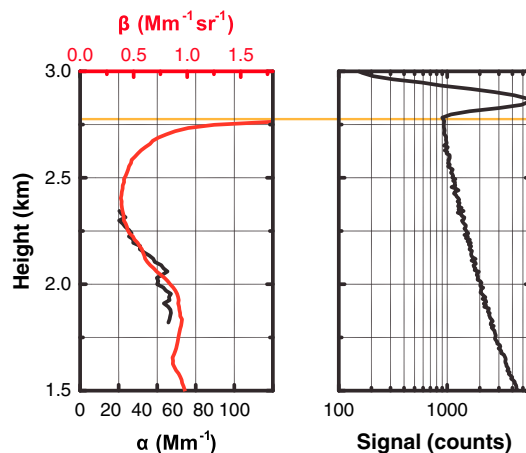


Figure 10. (left) Profiles of the particle extinction (black) and backscatter coefficient (red) measured on 15 August 2011, 20:29–21:30 UTC average. (right) Signal profile from the outer FOV at 607 nm (Raman multiple-scattering channel, 20:29–20:46 UTC average) indicating a cloud at 2.8 km height (cloud base). The increasing relative humidity below the cloud layer leads to a strong increase of the backscatter coefficient by a factor of about 5 from 2.3 to 2.755 km (99% relative-humidity height level). Cloud top temperature was 0.5°C around 3.0 km height.

The backscatter profile shows an almost textbook-like increase between 2.4 and 2.75 km height caused by particle water uptake. Particle extinction coefficient ranged from 20 to 50 Mm^{-1} between 1.5 and 2.5 km height.

The vertical wind velocity at cloud base and in the lower part of the altocumulus layer obtained with the Doppler lidar for the selected 16 min cloud observation is presented in Figure 11 (top). Corresponding vertical wind statistics are shown in Figure 11 (bottom). The updraft and downdraft speeds were mostly <0.5 m/s.

The dual-FOV Raman lidar was run with FOVs of 0.5 and 2.0 mrad. The cloud observations in Figure 12 were sorted according to the occurrence of updrafts and downdrafts. A dual-FOV Raman signal profile was assigned to an updraft or downdraft region if the corresponding vertical velocity showed a positive or negative value at cloud base, respectively. Eighty-three updraft-related and 123 downdraft-related MARTHA signal profiles (each accumulated over 4 s) were added and averaged. Afterward, the cloud retrieval algorithm

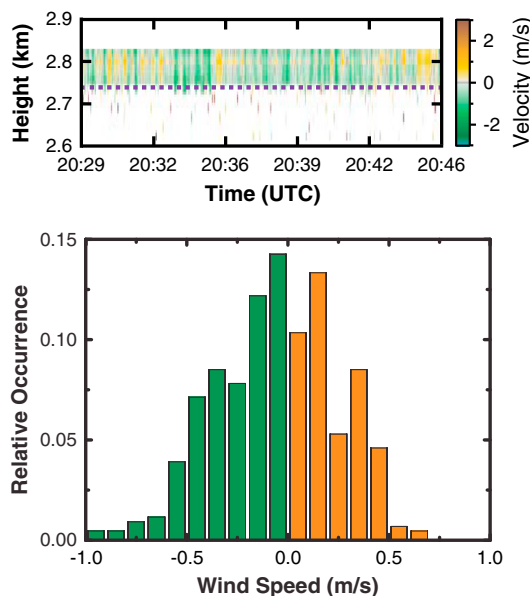


Figure 11. (top) Vertical wind velocity at cloud base and in the lower cloud part measured with Doppler lidar on 15 August 2011, 20:29–20:46 UTC. (bottom) Relative occurrence of measured vertical wind velocities (downdrafts in green, updrafts in orange) at cloud base during the time period shown in the top panel.

most of vertical wind velocities (70%) were in the range from -0.2 m/s to 0.2 m/s. On 15 August 2011, such low wind speeds were found in only 50% out of all cases. Less strong vertical motions on 29 August 2011 may be favorable for other effects to become dominant, e.g., downward mixing of dry air from above the shallow cloud layer.

Seventy-four and one hundred 4 s profiles recorded during updraft and downdraft periods, respectively, were used for the data analysis of 29 August 2011. Aerosol particle extinction coefficients were as high as 70 Mm^{-1} within an 800 m thick aerosol layer (200 to 1000 m below cloud base), and the minimum value was close to 45 Mm^{-1} just below the cloud base. Backward trajectory analysis indicates a slow aerosol transport at low heights from Spain over France and southwestern Germany toward Leipzig (for aerosol arriving at heights around 2000 m) and thus accumulation of aged anthropogenic haze particles. In contrast, on 15 August 2011, a comparably fast air mass transport occurred and the aerosol particles traveled at heights of 2000–3000 m from the Atlantic, crossed Belgium and western Germany before arriving at Leipzig (at about 3500 m height). In this case a composition of less aged European haze of low concentration mixed with free-tropospheric background aerosol dominated.

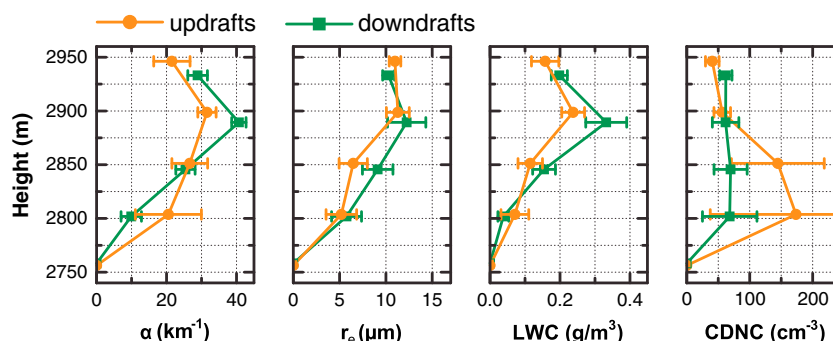


Figure 12. Cloud microphysical properties retrieved from the dual-FOV Raman lidar observations during updraft (orange) and downdraft (green) periods on 15 August 2011, 20:29–20:46 UTC.

was applied to both data signal sets separately to derive the cloud microphysical parameters as shown in Figure 12. The applied signal averaging is necessary to reduce the influence of signal noise on the uncertainty in the cloud retrieval products to an acceptable level.

A clear difference in the cloud properties for updraft and downdraft times is especially visible in terms of droplet extinction coefficient and CDNC at the lowermost height level within the cloud layer. The strong increase of the extinction coefficient and CDNC can be attributed to new droplet formation. Slightly lower cloud effective radii in the ascending air are consistent with this hypothesis. The LWC profile for the updraft times (orange profile) is in agreement with the respective adiabatic LWC profile. Again deviations from the adiabatic LWC profile are observed for the downward times (green profile, too large values).

A second example of combined dual-FOV and Doppler lidar is shown in Figure 13. Less strong updraft and downdraft motions were observed on 29 August 2011. The histogram of the measured vertical wind velocities (not shown) indicated that

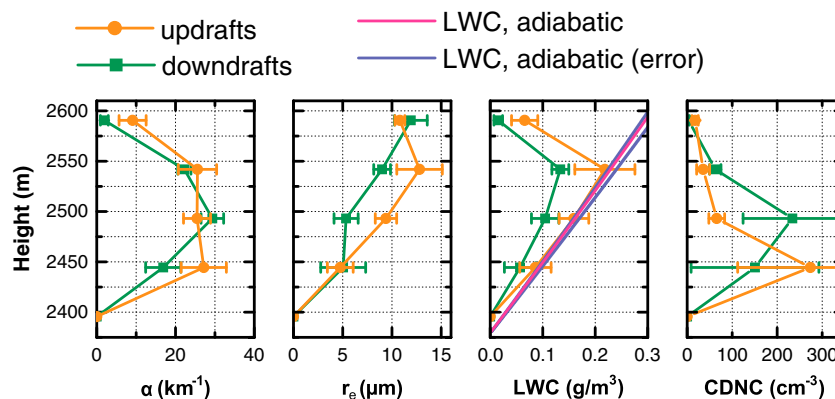


Figure 13. Cloud microphysical properties retrieved from the dual-FOV Raman lidar observations during updraft (orange) and downdraft (green) periods on 29 August 2011, 20:59–21:18 UTC. The calculated profile of the adiabatic LWC is shown in pink with purple lines indicating the error margin.

The cloud products presented in Figure 13 differ considerably from the findings in the preceding Figure 12. Higher values of cloud extinction coefficient and CDNC were observed on this day with the higher aerosol load. The aerosol particle extinction coefficients below the cloud layer were about a factor of 2 smaller on 15 August compared to the conditions on 29 August 2011. Lower effective radii and lower LWC values were observed around cloud center during the downdraft periods on 29 August. Turbulent mixing and associated entrainment of dry air from above and subsequent evaporation of the small droplet fraction is consistent with this finding.

To corroborate the hypothesis of dry air entrainment, the adiabatic LWC profile is explicitly shown here. For this calculation an accurate knowledge of the cloud base height and cloud base temperature is necessary. The microwave radiometer HATPRO allows us to estimate the temperature profile. The accuracy of this retrieval is about 1.5 K in an altitude range around 2.4 km height [Löhnert and Maier, 2012]. A temperature of $-0.2 \pm 1.5^\circ\text{C}$ was obtained at cloud base. For comparison, the simulated GDAS temperature at cloud base height was 0°C for grid point Leipzig at 21:00 UTC on 29 August 2011. The computed profile of the adiabatic LWC presented in Figure 13 suggests an adiabatic increase for the updraft times which is reasonable when droplet growth through condensation dominates. For the downdraft times, the subadiabatic LWC profile is consistent with entrainment of dry air from above.

Kim *et al.* [2008] summarized the complications in ACI studies by turbulent motions as follows. Strong turbulent mixing may lead to strong evaporation of droplets associated with a strong reduction in CDNC and an increase of the droplet effective radius because of predominant evaporation of small droplets. Stronger turbulence within the cloud may, on the other hand, increase drop collisions with the result that CDNC decreases and effective radius increases. Strong updrafts may cause new droplet formation (leading to a decrease of effective radius) and/or growth of large droplets on the expense of smaller ones (leading to an increase of effective radius). Our observations in Figures 12 and 13 clearly corroborate the conclusions of Kim *et al.* [2008] that turbulent mixing reduces the aerosol effect on CDNC. From these reasons, studies of the aerosol-cloud relationship based on measured cloud column parameters (or cloud mean values of effective radius and CDNC) of layered clouds must be interpreted with caution. The specific impact of varying aerosol conditions cannot be separated from meteorological aspects. The latter may dominate the evolution of a cloud layer and widely determine the cloud microphysical and optical properties.

We finally compared the two August 2011 measurements (with similar LWC conditions in the lower cloud parts) and calculated several ACI_N values. Figure 14 provides an overview of the aerosol and cloud observations, relevant for our ACI_N computation. In the ACI_N computation, we distinguished four scenarios: (a) ACI_N calculation with cloud properties at the lowest height level and by considering updraft periods only, (b) same as scenario (a) but including all (updraft and downdraft) periods in the ACI_N computation, (c) ACI_N calculation with vertical mean cloud properties considering updraft periods only, and (d) same as scenario (c) but including all (updraft and downdraft) periods in the calculation. As aerosol proxy we used the minimum particle extinction coefficients in Figure 14 of 20 Mm^{-1} (15 August) and 45 Mm^{-1} (29 August). For scenarios

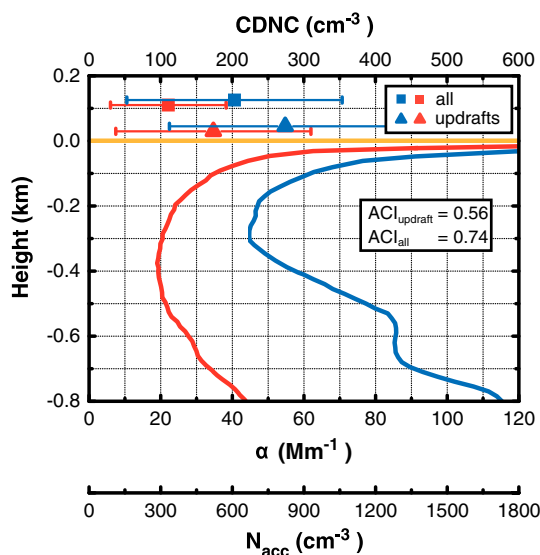


Figure 14. Aerosol-cloud relationship in terms of ACI_N based on lidar-derived particle extinction profiling below cloud base (solid lines) and CDNCs just above cloud base (symbols, same as the values in Figures 12 and 13 for the lowest height level). The orange line indicates cloud base and defines height level of 0 m for the particle extinction profiles, measured on 15 August (red, same as in Figure 10) and on 29 August 2011 (blue). Extinction coefficients are computed from respective backscatter coefficients multiplied with an aerosol particle lidar ratio of 50 sr. The N_{acc} scaling (second x axis) assumes that an extinction coefficient of 50 Mm^{-1} corresponds to an accumulation-mode particle concentration of 750 cm^{-3} . In the computation of indicated CDNC and ACI_N values, dual-FOV lidar observations of cloud properties just above cloud base (also shown in Figures 12 and 13) are used, for the entire cloud period (all: updraft + downdraft periods; updraft: updraft periods only). In the computation of ACI_N , minimum particle extinction values of 20 Mm^{-1} (red) and 45 Mm^{-1} (blue) are considered.

(c) and (d), Table 1 indicates very different LWP conditions with $7.6\text{--}12.9 \text{ g/m}^2$ on 29 August 2011 and $27.7\text{--}31.6 \text{ g/m}^2$ on 15 August 2011. For such variable LWP conditions only the computation of ACI_N may lead to useful results.

For optimum conditions (scenario (a), use of cloud-base cloud parameters, and consideration of updraft periods only), we obtain $ACI_N=0.56$. If we ignore the wind information (scenario (b)), we yield $ACI_N=0.77$. When using vertical mean cloud properties, we obtain $ACI_N=0.37$ (for scenario (c), for updraft periods only) and $ACI_N = -0.055$ (scenario (d), wind information ignored). Surprisingly, ACI_N for scenario (b) is larger than the values for the optimum scenario (a). This is caused in the shown case by the fact that the absolute CDNCs are lower in both measurement cases when the wind information is ignored, but the absolute difference between the two values remains almost the same and does not depend whether we use updraft periods only or the entire time interval in the analysis. The ACI_N parameter however is a function of the relative CDNC difference which is then higher for the lower absolute CDNC values.

For comparison, average values of airborne in situ observation for ACI_N were close 0.55 [Lu et al., 2007; Terai et al., 2012]. As an exception, Painemal and Zuidema [2013] found even larger values of 0.76–0.92. In these airborne field campaigns of marine layered clouds, flights were not sorted according to different flight levels within the cloud layer (base, center, and top level) and all these observations were then equally considered in the ACI studies, i.e., without distinguishing

between the different height levels above cloud base. This kind of averaging probably also leads to an underestimation of the aerosol effect (as mentioned, most clearly visible only in the lowest cloud part).

By assuming that scenario (a) provides optimum conditions for the ACI quantification, we see that the other three scenarios (b)–(d) differ significantly (35%–100%) from the optimum value of 0.56 in this case study. In agreement with Kim et al. [2008], we may conclude that downdrafts and turbulent mixing immediately begin to reduce any clear aerosol impact on cloud microphysical properties on the way up through the cloud layer. This hypothesis is already mentioned in earlier publications and corroborated by the review of McComiskey and Feingold [2008]. The authors summarize different ACI studies performed since 1993 and found a wide spread of ACI_N from close to 0.1–1.0. McComiskey et al. [2009] then presented a study of ground-based aerosol characterization and remote sensing of column-integrated cloud properties (effective radius, CDNC) of coastal stratocumulus over California and found a mean value of $ACI_N=0.48$ when considering only values within a physically plausible range of 0–1.0. However, they found also many values between –2 and 2. On average, they observed the strongest ACI values during updraft times (mean value of 0.58 for updraft $>0.5 \text{ m/s}$ and of 0.69 for updrafts $>1 \text{ m/s}$).

The smallest ACI_N values (global means) of 0.08 over land and 0.25 over the oceans are finally obtained in the case of satellite remote sensing [Quaas et al., 2009] in which horizontally averaged aerosol optical depths (for ambient conditions) are set into context with cloud column properties which are also averaged over large areas and which are furthermore dominated by the radiative information from cloud top regions. Horizontal averaging not only smooth out the updraft effects on ACI_N but also inhomogeneities in the

aerosol distribution and cloud LWP variability. For completeness, the strong variability in all of the published ACI_N numbers also reflects the influence of uncertainties in the measurements, in the selected observation strategies, and mismatched sampling of aerosol and cloud properties in space and time.

The limitations of lidar were already mentioned in section 1. With focus on the uncertainties in the ACI_N determination, Figure 14 indicates the large uncertainties in the CDNC values. The aerosol parameter used in Figure 14 is the particle extinction coefficient. As mentioned above, this is the most robust aerosol quantity we can measure with lidar. The best aerosol parameter would be APNC (see the second x axis in Figure 14). The relationship between α_p and APNC is however not straightforward. For the same α_p , APNC can vary by a factor of 2–3 or even more as a result of a varying aerosol size distribution (and absorption and scattering conditions). This must be considered as an important source of uncertainty in the ACI_N estimation. We checked the Ångström exponents (describing the spectral slopes of α_p) of the backscatter and extinction coefficients. The Ångström exponent sensitively changes with a change in the aerosol particle size distribution. We found similar Ångström exponents for 15 and 29 August 2011 so that we assume that α_p was well correlated with APNC for these two cases so that our ACI_N estimates in Figure 14 are quite accurate. After the evaluation of all data (of 20–30 cloud cases) we may draw more solid conclusions concerning ACI over polluted continents and the role of updraft knowledge.

4. Conclusions and Outlook

A new lidar technique was introduced that allows simultaneous profiling of aerosol and warm-cloud optical and microphysical properties. An unambiguous cloud base detection is now possible by using the multiple-scattering channel of the new dual-FOV Raman lidar. In combination with a Doppler lidar for vertical-wind observations, the dual-FOV lidar was used to investigate the influence of aerosol particles on cloud properties of layered, purely liquid clouds in the lower free troposphere over a polluted, central European site.

In three case studies the key findings of our 3 year observational period were discussed. The potential to determine relationships between CDNC and APNC (particles with diameters > 100 nm) at ambient humidity conditions solely from the dual-FOV Raman lidar observations was illuminated. The impact of updraft and downdraft motion on the parameter ACI_N describing the relationship between CDNC and aerosol load below cloud base was highlighted. The combined lidar observations corroborate that ACI values are highest at cloud base, and the use of cloud-mean properties blurs and reduces the measurable effect on cloud properties. Vertical mixing and dry-air entrainment cause significant reduction of a clear and direct aerosol effect on cloud microphysical properties with increasing height above cloud base. In a follow-up paper we will present the statistics of our 3 year observations of layered clouds.

Acknowledgments

The presented work was facilitated by the support of the whole group for ground-based remote sensing of the TROPOS Institute. Fruitful discussions with Florian Ditas contributed to the work. The research leading to these results has received funding from the European Union Seventh Framework Programme (FP7/2007–2013) under grant agreement 262254 (Aerosols, Clouds, and Trace gases Research Infrastructure Network, ACTRIS).

References

- Ansmann, A., and D. Müller (2005), Lidar and atmospheric aerosol particles, in *Lidar: Range-Resolved Optical Remote Sensing of the Atmosphere*, edited by C. Weitkamp, pp. 105–141, Springer, New York.
- Ansmann, A., M. Riebesell, and C. Weitkamp (1990), Measurement of atmospheric aerosol extinction profiles with a Raman lidar, *Opt. Lett.*, *15*, 746–748.
- Ansmann, A., M. Riebesell, U. Wandinger, C. Weitkamp, E. Voss, W. Lahmann, and W. Michaelis (1992), Combined raman elastic-backscatter lidar for vertical profiling of moisture, aerosol extinction, backscatter, and LIDAR ratio, *Appl. Phys. B*, *55*(1), 18–28, doi:10.1007/BF00348608.
- Ansmann, A., I. Mattis, D. Müller, U. Wandinger, M. Radlach, D. Althausen, and R. Damoah (2005), Ice formation in Saharan dust over central Europe observed with temperature/humidity/aerosol Raman lidar, *J. Geophys. Res.*, *110*, D18S12, doi:10.1029/2004JD005000.
- Ansmann, A., M. Tesche, P. Seifert, D. Althausen, R. Engelmann, J. Fruntke, U. Wandinger, I. Mattis, and D. Müller (2009), Evolution of the ice phase in tropical altocumulus: SAMUM lidar observations over Cape Verde, *J. Geophys. Res.*, *114*, D17208, doi:10.1029/2008JD011659.
- Bissonnette, L. R. (2005), Lidar and multiple scattering, in *LIDAR: Range-resolved Optical Remote Sensing of the Atmosphere*, edited by C. Weitkamp, pp. 43–103, Springer, New York.
- Bissonnette, L. R., and D. L. Hutt (1995), Multiply scattered aerosol lidar returns: Inversion method and comparison with in situ measurements, *Appl. Opt.*, *34*, 6959–6975.
- Bissonnette, L. R., G. Roy, L. Poutier, S. G. Cober, and G. A. Isaac (2002), Multiple-scattering lidar retrieval method: Tests on Monte Carlo simulations and comparisons with in situ measurements, *Appl. Opt.*, *41*, 6307–6324.
- Brenguier, J. L., H. Pawlowska, L. Schüller, R. Preusker, J. Fischer, and Y. Fouquart (2000), Radiative properties of boundary layer clouds: Droplet effective radius versus number concentration, *J. Atmos. Sci.*, *57*, 803–821, doi:10.1034/j.1600-0889.2000.00047.x.
- Bühl, J., R. Engelmann, and A. Ansmann (2012), Removing the laser-chirp influence from coherent Doppler lidar datasets by two-dimensional deconvolution, *J. Atmos. Oceanic Technol.*, *29*(8), 1042–1051.

- Bühl, J., A. Ansmann, P. Seifert, H. Baars, and R. Engelmann (2013), Toward a quantitative characterization of heterogeneous ice formation with lidar/radar: Comparison of CALIPSO/CloudSat with ground-based observations, *Geophys. Res. Lett.*, *40*, 4404–4408, doi:10.1002/grl.50792.
- Crewell, S., and U. Löhnert (2003), Accuracy of cloud liquid water path from ground-based microwave radiometry 2. Sensor accuracy and synergy, *Radio Sci.*, *38*(3), 8042, doi:10.1029/2002RS002634.
- Deirmendian, D. (1969), *Electromagnetic Scattering of Spherical Polydispersions*, 290 pp., Elsevier, New York.
- DeMott, P. J., A. J. Prenni, X. Liu, S. M. Kreidenweis, M. D. Petters, C. H. Twohy, M. S. Richardson, T. Eidhammer, and D. C. Rogers (2010), Predicting global atmospheric ice nuclei distributions and their impacts on climate, *Proc. Natl. Acad. Sci. U.S.A.*, *107*, 11,217–11,222, doi:10.1073/pnas.0910818107.
- Ditas, F., R. A. Shaw, H. Siebert, M. Simmel, B. Wehner, and A. Wiedensohler (2012), Aerosols-cloud microphysics-thermodynamics-turbulence: Evaluating supersaturation in a marine stratocumulus cloud, *Atmos. Chem. Phys.*, *12*(5), 2459–2468, doi:10.5194/acp-12-2459-2012.
- Ebell, K., S. Crewell, U. Löhnert, D. D. Turner, and E. J. O'Connor (2011), Cloud statistics and cloud radiative effect for a low-mountain site, *Q. J. R. Meteorol. Soc.*, *137*(S1), 306–324, doi:10.1002/qj.748.
- Eidhammer, T., et al. (2010), Ice initiation by aerosol particles: Measured and predicted ice nuclei concentrations versus measured ice crystal concentrations in an orographic wave cloud, *J. Atmos. Sci.*, *67*, 2417–2436, doi:10.1175/2010JAS3266.1.
- Engelmann, R., U. Wandinger, A. Ansmann, D. Müller, E. Zeromskis, D. Althausen, and B. Wehner (2008), Lidar observations of the vertical aerosol flux in the planetary boundary layer, *J. Atmos. Oceanic Technol.*, *25*, 1296–1306.
- Feingold, G. (2003b), Modeling of the first indirect effect: Analysis of measurements requirements, *Geophys. Res. Lett.*, *30*(19), 1997, doi:10.1029/2003GL017967.
- Feingold, G., L. Remer, J. Ramaprasad, and Y. Kaufman (2001), Analysis of smoke impact on clouds in Brazilian biomass burning regions: An extension of Twomey's approach, *J. Geophys. Res.*, *106*(D19), 22,907–22,922, doi:10.1029/2001JD000732.
- Feingold, G., W. L. Eberhard, D. E. Veron, and M. Previdi (2003a), First measurements of the Twomey indirect effect using ground-based remote sensors, *Geophys. Res. Lett.*, *30*(6), 1287, doi:10.1029/2002GL016633.
- Feingold, G., R. Furrer, P. Pilewskie, L. A. Remer, Q. Min, and H. Jonsson (2006), Aerosol indirect effect studies at Southern Great Plains during the May 2003 Intensive Operations Period, *J. Geophys. Res.*, *111*, D05S14, doi:10.1029/2004JD005648.
- Field, P. R., A. J. Heymsfield, B. J. Shipway, P. J. DeMott, K. A. Pratt, D. C. Rogers, J. Stith, and K. A. Prather (2011), Ice in clouds experiment–layer clouds. Part II: Testing characteristics of heterogeneous ice formation in lee wave clouds, *J. Atmos. Sci.*, *69*, 1066–1079, doi:10.1175/JAS-D-11-026.1.
- Forster, P., et al. (2007), Changes in atmospheric constituents and in radiative forcing, in *Climate Change 2007: The Physical Science Basis. Contribution of Working Group I to the Fourth Assessment Report of the Intergovernmental Panel on Climate Change*, chap. 2, edited by S. Solomon et al., Cambridge Univ. Press, Cambridge, U. K.
- Garrett, T. J., C. Zhao, X. Dong, G. G. Mace, and P. V. Hobbs (2004), Effects of varying aerosol regimes on low-level Arctic stratus, *Geophys. Res. Lett.*, *31*, L17105, doi:10.1029/2004GL019928.
- Gaussiat, N., R. J. Hogan, and A. J. Illingworth (2007), Accurate liquid water path retrieval from low-cost microwave radiometers using additional information from a lidar ceilometer and operational forecast models, *J. Atmos. Oceanic Technol.*, *24*, 1562–1575.
- Illingworth, A. J., et al. (2007), CLOUDNET: Continuous evaluation of cloud profiles in seven operational modes using ground-based observations, *Bull. Am. Meteorol. Soc.*, *88*, 883–898.
- Kanamitsu, M. (1989), Description of the NMC global data assimilation and forecast system, *Weather and Forecasting*, *4*, 335–342, doi:10.1175/1520-0434(1989)004<0335:DOTNGD>2.0.CO;2.
- Kanitz, T., P. Seifert, A. Ansmann, R. Engelmann, D. Althausen, C. Casaccia, and E. G. Rohwer (2011), Contrasting the impact of aerosols at northern and southern midlatitudes on heterogeneous ice formation, *Geophys. Res. Lett.*, *38*, L17802, doi:10.1029/2011GL048532.
- Kim, B.-G., S. E. Schwartz, and M. A. Miller (2003), Effective radius of cloud droplets by ground-based remote sensing: Relationship to aerosol, *J. Geophys. Res.*, *108*(D23), 4740, doi:10.1029/2003JD003721.
- Kim, B.-G., M. A. Miller, S. E. Schwartz, Y. Liu, and Q. Min (2008), The role of adiabaticity in the aerosol first indirect effect, *J. Geophys. Res.*, *113*, D05210, doi:10.1029/2007JD008961.
- Kleinman, L. I., et al. (2012), Aerosol concentration and size distribution measured below, in, and above cloud from the DOE G-1 during VOCALS-REx, *Atmos. Chem. Phys.*, *12*(1), 207–223, doi:10.5194/acp-12-207-2012.
- Löhnert, U., and O. Maier (2012), Operational profiling of temperature using ground-based microwave radiometry at payerne: Prospects and challenges, *Atmos. Meas. Tech.*, *5*, 1121–1134, doi:10.5194/amt-5-1121-2012.
- Lu, M. L., and J. H. Seinfeld (2006), Effect of aerosol number concentration on cloud droplet dispersion: A large-eddy simulation study and implications for aerosol indirect forcing, *J. Geophys. Res.*, *111*, D02207, doi:10.1029/2005JD006419.
- Lu, M.-L., W. C. Conant, H. H. Jonsson, V. Varutbangkul, R. C. Flagan, and J. H. Seinfeld (2007), The marine stratus/stratocumulus experiment (MASE): Aerosol-cloud relationship in marine stratocumulus, *J. Geophys. Res.*, *112*, D10209, doi:10.1029/2006JD007985.
- Malinka, A. V., and E. P. Zege (2003), Analytical modeling of Raman lidar return, including multiple scattering, *Appl. Opt.*, *42*, 1075–1080.
- Malinka, A. V., and E. P. Zege (2007), Possibilities of warm cloud microstructure profiling with multiple-field-of-view Raman lidar, *Appl. Opt.*, *46*, 8419–8427.
- Martin, G. M., D. W. Johnson, and A. Spice (1994), The measurement and parameterization of effective radius of droplets in warm stratocumulus clouds, *J. Atmos. Sci.*, *51*(13), 1823–1842, doi:10.1175/1520-0469(1994)051<1823:TMAPOE>2.0.CO;2.
- Martucci, G., and C. D. O'Dowd (2011), Ground-based retrieval of continental and marine warm cloud microphysics, *Atmos. Meas. Tech.*, *4*, 2749–2765, doi:10.5194/amt-4-2749-2011.
- Mattis, I., A. Ansmann, D. Müller, U. Wandinger, and D. Althausen (2004), Multiyear aerosol observations with dual-wavelength Raman lidar in the framework of EARLINET, *J. Geophys. Res.*, *109*, D13203, doi:10.1029/2004JD004600.
- Mattis, I., D. Müller, A. Ansmann, U. Wandinger, J. Preissler, P. Seifert, and M. Tesche (2008), Ten years of multiwavelength Raman lidar observations of free-tropospheric aerosol layers over central Europe: Geometrical properties and annual cycle, *J. Geophys. Res.*, *113*, D20202, doi:10.1029/2007JD009636.
- Mattis, I., P. Seifert, D. Müller, M. Tesche, A. Hiesch, T. Kanitz, J. Schmidt, F. Finger, U. Wandinger, and A. Ansmann (2010), Volcanic aerosol layers observed with multiwavelength Raman lidar over central Europe in 2008–2009, *J. Geophys. Res.*, *115*, D00L04, doi:10.1029/2009JD013472.
- McComiskey, A., and G. Feingold (2008), Quantifying error in the radiative forcing of the first aerosol indirect effect, *Geophys. Res. Lett.*, *35*, L02810, doi:10.1029/2007GL032667.

- McComiskey, A., G. Feingold, A. S. Frisch, D. D. Turner, M. A. Miller, J. C. Chiu, Q. Min, and J. A. Ogren (2009), An assessment of aerosol-cloud interactions in marine stratus clouds based on surface remote sensing, *J. Geophys. Res.*, *114*, D09203, doi:10.1029/2008JD011006.
- Miles, N., J. Verlinde, and E. Clothiaux (2000), Cloud droplet size distributions in low-level stratiform clouds, *J. Atmos. Sci.*, *57*(2), 295–311.
- Müller, D., U. Wandinger, and A. Ansmann (1999), Microphysical particle parameters from extinction and backscatter lidar data by inversion with regularization: Theory, *Appl. Opt.*, *38*(12), 2346–2357, doi:10.1364/AO.38.002346.
- Müller, D., I. Mattis, U. Wandinger, A. Ansmann, D. Althausen, and A. Stohl (2005), Raman lidar observations of aged Siberian and Canadian forest fire smoke in the free troposphere over Germany in 2003: Microphysical particle characterization, *J. Geophys. Res.*, *110*, D17201, doi:10.1029/2004JD005756.
- Müller, D., A. Ansmann, I. Mattis, M. Tesche, U. Wandinger, D. Althausen, and G. Pisani (2007), Aerosol-type-dependent lidar ratios observed with Raman lidar, *J. Geophys. Res.*, *112*, D16202, doi:10.1029/2006JD008292.
- Painemal, D., and P. Zuidema (2013), The first aerosol indirect effect quantified through airborne remote sensing during VOCALS-REx, *Atmos. Chem. Phys.*, *13*, 917–931, doi:10.5194/acp-13-917-2013.
- Plass, G. N., and G. W. Kattawar (1971), Reflection of light pulses from clouds, *Appl. Opt.*, *10*, 2304–2310.
- Quaas, J., et al. (2009), Aerosol indirect effects – general circulation model intercomparison and evaluation with satellite data, *Atmos. Chem. Phys.*, *9*, 8697–8717, doi:10.5194/acp-9-8697-2009.
- Rose, T., S. Crewell, U. Löhnert, and C. Simmer (2005), A network suitable microwave radiometer for operational monitoring of the cloudy atmosphere, *Atmos. Res.*, *75*, 183–200, doi:10.1016/j.atmosres.2004.12.005.
- Rosenfeld, D., M. Clavner, and R. Nirel (2011), Pollution and dust aerosols modulating tropical cyclones intensities, *Atmos. Res.*, *102*, 66–76, doi:10.1016/j.atmosres.2011.06.006.
- Schmidt, J., U. Wandinger, and A. Malinka (2013), Dual-field-of-view Raman lidar measurements for the retrieval of cloud microphysical properties, *Appl. Opt.*, *52*(11), 2235–2247.
- Seifert, P., A. Ansmann, D. Müller, U. Wandinger, D. Althausen, A. J. Heymsfield, S. T. Massie, and C. Schmitt (2007), Cirrus optical properties observed with lidar, radiosonde, and satellite over the tropical Indian Ocean during the aerosol-polluted northeast and clean maritime southwest monsoon, *J. Geophys. Res.*, *112*, D17205, doi:10.1029/2006JD008352.
- Shupe, M. D. (2007), A ground-based multisensor cloud phase classifier, *Geophys. Res. Letts.*, *34*, L22809, doi:10.1029/2007GL031008.
- Terai, C. R., R. Wood, D. C. Leon, and P. Zuidema (2012), Does precipitation susceptibility vary with increasing cloud thickness in marine stratocumulus?, *Atmos. Chem. Phys.*, *12*, 4567–4583, doi:10.5194/acp-12-4567-2012.
- Twohy, C., M. Petters, J. Snider, B. Stevens, W. Tahnk, M. Wetzell, L. Russell, and F. Burnet (2005), Evaluation of the aerosol indirect effect in marine stratocumulus clouds: Droplet number, size, liquid water path, and radiative impact, *J. Geophys. Res.*, *110*, D08203, doi:10.1029/2004JD005116.
- Twohy, C. H., et al. (2013), Impacts of aerosol particles on the microphysical and radiative properties of stratocumulus clouds over the southeast Pacific Ocean, *Atmos. Chem. Phys.*, *13*, 2541–2562, doi:10.5194/acp-13-2541-2013.
- Veselovskii, I., M. Korenskii, V. Griaznov, D. N. Whiteman, M. McGill, G. Roy, and L. Bissonnette (2006), Information content of data measured with a multiple-field-of-view lidar, *Appl. Opt.*, *45*(26), 6839–6848.
- Wandinger, U., et al. (2002), Optical and microphysical characterization of biomass-burning and industrial-pollution aerosols from multiwavelength lidar and aircraft measurements, *J. Geophys. Res.*, *107*(D21), 8125, doi:10.1029/2000JD000202.
- Wandinger, U., et al. (2004), Air mass modification over Europe: EARLINET aerosol observations from Wales to Belarus, *J. Geophys. Res.*, *109*, D24205, doi:10.1029/2004JD005142.
- Wandinger, U., et al. (2012), Integrated remote-sensing techniques to study aerosols, clouds, and their interaction, paper presented at 26th International Laser Radar Conference, vol. I, pp. 395–398, Porto Heli, Greece, 25–29 June 2012.
- Westwater, E., Y. Han, M. Shupe, and S. Matrosov (2001), Analysis of integrated cloud liquid and precipitable water vapor retrievals from microwave radiometers during the Surface Heat Budget of the Arctic Ocean project, *J. Geophys. Res.*, *106*(D23), 32,019–32,030.